AFRL-AFOSR-VA-TR-2019-0149

Thermoelectric Phenomena in Quasi-One-Dimensional Metals

Katayun Barmak
THE TRUSTEES OF COLUMBIA UNIVERSITY IN THE CITY OF NEW YORK
116TH AND BDWY
NEW YORK, NY 10027

06/13/2019
Final Report

Air Force Research Laboratory
AF Office Of Scientific Research (AFOSR)/ION

Arlington, Virginia 22203
Air Force Materiel Command

REPORT DOCUMENTATION PAGE

Form Approved
OMB No. 0704-0188

1. REPORT DATE *(DD-MM-YYYY)*	2. REPORT TYPE	3. DATES COVERED *(From - To)*
13-06-2019	Final	15 Dec 2017 to 14 Dec 2019

4. TITLE AND SUBTITLE
Thermoelectric Phenomena in Quasi-One-Dimensional Metals

5a. CONTRACT NUMBER

5b. GRANT NUMBER
FA9550-18-1-0063

5c. PROGRAM ELEMENT NUMBER
61102F

6. AUTHOR(S)
Katayun Barmak

5d. PROJECT NUMBER

5e. TASK NUMBER

5f. WORK UNIT NUMBER

7. PERFORMING ORGANIZATION NAME(S) AND ADDRESS(ES)
THE TRUSTEES OF COLUMBIA UNIVERSITY IN THE CITY OF NEW YORK
116TH AND BDWY
NEW YORK, NY 10027 US

8. PERFORMING ORGANIZATION REPORT NUMBER

9. SPONSORING/MONITORING AGENCY NAME(S) AND ADDRESS(ES)
AF Office of Scientific Research
875 N. Randolph St. Room 3112
Arlington, VA 22203

10. SPONSOR/MONITOR'S ACRONYM(S)
AFRL/AFOSR ION

11. SPONSOR/MONITOR'S REPORT NUMBER(S)
AFRL-AFOSR-VA-TR-2019-0149

12. DISTRIBUTION/AVAILABILITY STATEMENT
A DISTRIBUTION UNLIMITED: PB Public Release

13. SUPPLEMENTARY NOTES

14. ABSTRACT
Epitaxial Ru films with resistivities that approach the bulk resistivity in the thick film limit have been prepared. Methods have also been developed to controllably grow ultrathin silica capping layers over Ru(0001)-terminated films. The structure of the films with and without surface oxide layers was characterized by X-ray diffraction, X-ray reflectivity, X-ray photoelectron spectroscopy, low energy electron diffraction, (scanning) transmission electron microscopy and selected area electron diffraction. Highly specular electron surface scattering has been obtained for suitably processed (0001) Ru surfaces. The fabrication of nanowires from the single crystal films by focused He ion beam milling has been unsuccessful and efforts have recently been redirected to the more conventional electron beam lithography. A code based on the tight-binding approach for electronic band structure and electrical transport calculations has been developed. The code implements the KernelPolynomial method very efficiently, using an approach which scales linearly with the number of atomic sites.

15. SUBJECT TERMS
Ballistic Conductance

16. SECURITY CLASSIFICATION OF:			17. LIMITATION OF ABSTRACT	18. NUMBER OF PAGES	19a. NAME OF RESPONSIBLE PERSON
a. REPORT	b. ABSTRACT	c. THIS PAGE			POKINES, BRETT
Unclassified	Unclassified	Unclassified	SAR		19b. TELEPHONE NUMBER *(Include area code)* 703-588-1772

Standard Form 298 (Rev. 8/98)
Prescribed by ANSI Std. Z39.18

Thermoelectric Phenomena in Quasi-One-Dimensional Metals

FA9550-18-1-0063

12/15/2017 – 12/14/2018

Year 1 and Final Project Report

K. Barmak
Columbia University

K. R. Coffey, W. E. Kaden, E. Mucciolo, P. K. Schelling
University of Central Florida

The aim of the proposed work is a breakthrough demonstration of enhanced thermoelectric materials using a top-down approach to fabricate quasi one-dimensional metallic nanowires with a high degree of structural perfection to allow exploration of thermoelectric phenomena in the novel regime of ballistic conduction.

Abstract: Epitaxial Ru films with resistivities that approach the bulk resistivity in the thick film limit have been prepared. Methods have also been developed to controllably grow ultrathin silica capping layers over Ru(0001)-terminated films. The structure of the films with and without surface oxide layers was characterized by X-ray diffraction, X-ray reflectivity, X-ray photoelectron spectroscopy, low energy electron diffraction, (scanning) transmission electron microscopy and selected area electron diffraction. Highly specular electron surface scattering has been obtained for suitably processed (0001) Ru surfaces. The fabrication of nanowires from the single crystal films by focused He ion beam milling has been unsuccessful and efforts have recently been redirected to the more conventional electron beam lithography. A code based on the tight-binding approach for electronic band structure and electrical transport calculations has been developed. The code implements the Kernel-Polynomial method very efficiently, using an approach which scales linearly with the number of atomic sites.

1. Introduction and Background

The goal of this project is to explore thermoelectric phenomena in metallic, narrow (sub-10 nm), quasi-one-dimensional nanowires with a quantum ballistic limited electronic conductance of the order of 10^{15} $\Omega^{-1}m^{-2}$[1]. This yields a conductance of 10^{-2} Ω^{-1} for a 3×3 nm^2 wire, which is two orders of magnitude larger than that predicted for a perfect single-walled carbon nanotube [2] and three orders of magnitude larger than predicted for defect-free polycrystalline wires [3-7], defining a new regime in metal physics. We anticipate this regime will allow novel thermoelectric effects to be observed in metals and semi-metals that can be structurally integrated into aerospace components as a surface coating layer to provide multifunctional materials with thermoelectric energy harvesting and/or cooling effects. The utilization of the energy harvesting/and or cooling effects of quasi-one-dimensional metals is expected to "*promote the multifunctional design of*

advanced structures for superior thermal management and higher system efficiency in self-sustaining aerospace vehicles and platforms with unprecedented performance characteristics."

The research comprises the following efforts:

A) *An experimental effort on sub-10 nm nanowires and devices.*

B) *An experimental effort to characterize the nanowires and films at the atomic scale.*

C) *A theoretical physics and computational modeling effort to provide a quantitative understanding of ballistic transport in the size and defect limits, and serve to identify preferred metals for ballistic conductance for future efforts.*

Table 1 summarizes the efforts and for the thermoelectric studies proposed here and the associated teams. The five team members at Columbia University (CU) and the University of Central Florida (UCF) were chosen for their prior expertise in experimental studies of metal films and nanowires and in the theory and modeling of electron transport. They represent a comprehensive and complementary set of expertise and have a significant history of interactions and collaborations.

Table 1: Efforts and team members (function)

A)	Sample Preparation and Nanowire Thermoelectric Response	• Coffey – UCF (film growth, *ex situ* transport, nanowire patterning) • Barmak – CU (film growth) • Kaden – UCF (epitaxial dielectric growth, *in situ* transport)
B)	Defect and Structural Characterization	• Barmak – CU (TEM/STEM, electron tomography) • Coffey – UCF (X-ray diffraction/reflectivity) • Kaden – UCF (*in situ* characterization)
C)	Computational Modeling of Nanowire Conductance	• Mucciolo – UCF (transport code development and calculations) • Schelling – UCF (tight-binding model development)

The initial contract project contract was a 2-year contract, with year 2 as an option to be exercised. This option was not exercised, and, consequently, this report acts as both the Year 1 and the Final Project reports for the above referenced project FA9550-18-1-0063, including reports on deliverables from both Year 1 and 2 of the original proposal. The research effort is now continuing under a new project FA9550-19-1-0156.

Year 1

- Develop processing for high-quality, epitaxial metal films and nanowires with different crystallographic orientations and facets with epitaxial dielectric encapsulation (Efforts A and B).
- Provide tomographic and structural characterization and temperature-dependent transport data for the single crystal, oriented metal nanowires (Efforts A and B).

Year 2

- Provide tomographic and structural characterization and temperature-dependent transport and thermoelectric data for metal nanowires of varying thickness, wire width and crystallographic film and line orientation and crystal planes bounding the lines (Efforts A and B).
- Establish the basic physics of thermoelectric phenomena in the ballistic conduction regime. (Efforts A, B, and C)

Effort A) Sample Preparation and Nanowire Transport

In the Coffey group, c-axis single crystal Ru thin films on c-cut sapphire substrates were prepared. The epitaxial relationship was confirmed as $(0001)\,\mathrm{Ru} \| (0001)\,\mathrm{sapphire}$ and $[11\bar{2}0]\,\mathrm{Ru} \| [1\bar{1}00]\,\mathrm{sapphire}$, as has been reported in the literature.[8] The film thicknesses ranged from 8 nm to 124 nm and the films were deposited at temperatures ranging from 350-700 °C. *Ex situ* annealing as high as 950 °C has been shown to reduce film resistivity, with the thicker films having nearly bulk resistivity, as shown in Fig 1. These films were used as the basis for a study of surface scattering for the single crystal epitaxial Ru films and evidence of a primarily specular Ru/oxide interface was obtained.[9] Figure 1 plots the resistivity as a function of thickness for two series of single crystal Ru films that can be readily fit with the widely accepted Fuchs-Sondheimer (FS) resistivity size effect model [3,4] using an average specularity of zero ($p=0$) an EMFP, λ, of 6.7 nm and a bulk resistivity of 8.0 μΩ-cm. However, in this model, the EMFP and specularity are not independent parameters, as it is only the product, $\lambda \times (1-p)$, that is significant. This is clearly evident in the simplified version [3,4] of the FS model equation:

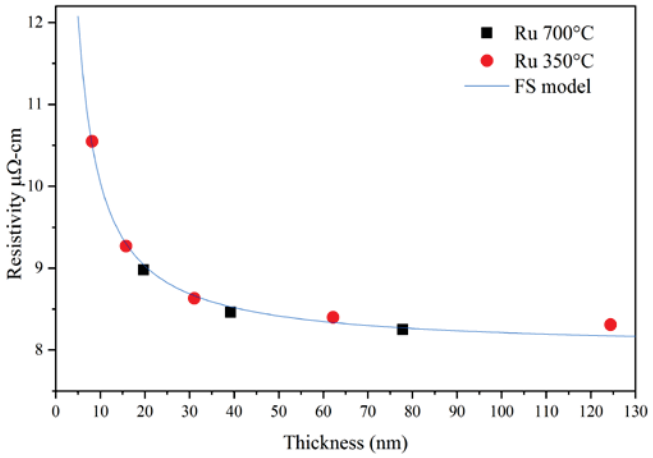

Fig. 1 – Resistivity versus thickness for c-axis single crystal Ru films deposited at 350 °C (circles) and 700 °C (squares) and ex-situ step-annealed to 950 °C in Ar/H_2 3%. The solid line is the calculation of the FS model.

$$\rho_{FS} = \rho_0 \left(1 + \left[\frac{3}{8}\frac{\lambda(1-p)}{h}\right]\right)$$

where ρ_{FS} is the resistivity of the thin film, ρ_o the resistivity of the material in bulk form, and h the thickness of the film. Table 2 provides examples of other choices of FS model parameters that would provide identical model predictions.

In a study focusing on surface structure for 20 nm thick Ru single crystal films, we found that the film resistivity increased with the room temperature deposition by sputtering or evaporation of an oxide on the Ru film surface. As such a deposition cannot generate defects within the layer, it disallows the p = 0 FS model parameter choice for the film prior to oxide deposition, as the resistivity increase cannot be attributed to an increase in surface scattering (i.e., a decrease in surface specularity) for a surface that is already fully diffuse. As only the scattering of the upper Ru surface is changed, FS model parameter combinations with an initially high upper surface specularity (e.g. 78%) can be used to describe the experimental observations.

Table 2 – Listing of FS model parameters.

EMFP λ, nm	Thick Film Resistivity ρ_o, μΩ-cm	Average Surface Specularity, p	Upper Surface Specularity p_U	Lower Surface Specularity p_L
6.7	8.0	0%	0%	0%
11.0	8.0	39%	39%	39%
11.0	8.0	39%	78%	0%
30.8	8.0	78%	78%	78%

The Ru metallic film thickness, RuO_x oxide layer thickness, Ru oxide to Ru metal intensity ratio (from X-ray photoelectron spectroscopy), Ru upper surface roughness, and variation of upper surface (Ru/SiO_2 interface) specularity at a series of sequential process steps is shown in Fig. 2. What is most notable is that the high upper surface specularity that is destroyed by the room temperature oxide deposition is restored by a subsequent reducing gas anneal of the bilayer film.

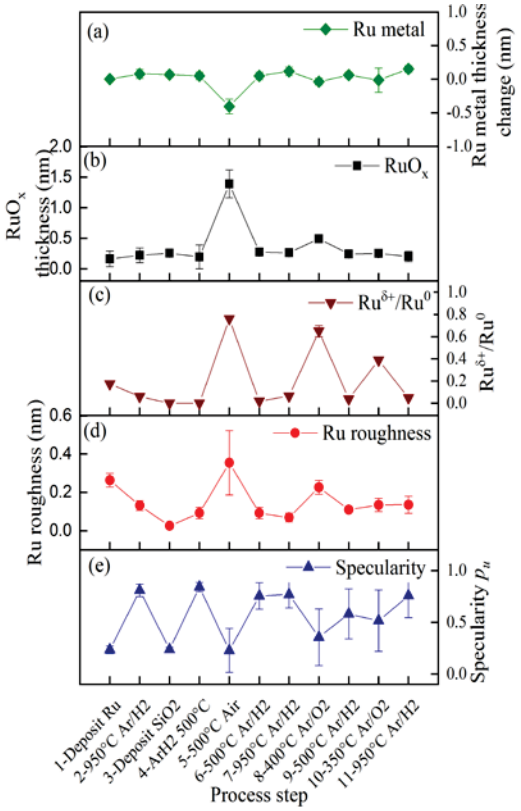

Fig. 2 - Plots showing (a) Ru metal thickness change, (b) RuO_x thickness, (c) Ru oxide to Ru metal ratio, (d) Ru upper surface roughness and (e) upper surface specularity (p) as a function of processing.

This work is continuing with a comparative examination of the resistivity effects of SiO_2, Al_2O_3, Cr_2O_3 and MgO. Similar resistivity increases for the room temperature deposition of SiO_2, Al_2O_3, Cr_2O_3 on annealed Ru films are observed, while for MgO a significantly greater resistivity increase occurs. Experiments to quantify the extent to which the specular surface is recovered are underway.

The Coffey group has also obtained epitaxial Ru single crystal films of other orientations, specifically Ru$\left(11\bar{2}0\right)$ and Ru $\left(1\bar{1}00\right)$ on other oxide single crystal substrates. These film orientations provide the Ru c-axis in the plane of the film and are important to explore conduction in different crystallographic directions, especially important for the case of Ru due to its inherent anisotropic conductivity in bulk single crystals. These orientations are not reported in the literature and our own initial efforts were unsuccessful due to the continued formation of c-axis and other, mixed orientations for the Ru films. More recently we have been successful with the use of a few monolayer deposits of a metallic seed layer on $\left(1\bar{1}00\right)$ and $\left(11\bar{2}0\right)$ sapphire substrates. The characterization of these films is shown below.

The Kaden group has succeeded in producing controllably grown, ultrathin silica capping layers over Ru(0001)-terminated films produced by the Coffey group. The films are grown via previously established physical vapor deposition approaches within UHV[10], and involve: (i) annealing the Ru/Al_2O_3 samples provided by the Coffey group at ~1300 K in ~1×10^{-5} Torr H_2 to reestablish surface cleanliness/order following exposure to air during transfer; (ii) formation of a 3O-2×2 patterned overlayer via exposure to 3×10^{-6} Torr O_2 at 1200 K for 5 minutes; (iii) controlled evaporative deposition of Si within an ~1×10^{-7} Torr O_2 atmosphere at ~100 K; and (iv) oxidative

crystallization of the film via repetition of step (ii). Both the Si concentration and the crystallization temperature are of central importance in determining the final characteristics of the film (crystalline vs. laterally amorphous vs. 3-dimensionally amorphous, and chemical-bound monolayers vs. physisorbed bilayers vs. bulk-like amorphous silica). Using these recipes, a highly ordered SiO_2/Ru(0001)/sapphire(0001) sample has been created for comparison with our recently published results from analogous samples capped with a thicker and amorphous silica layer. Results from that work will be described in more detail in our discussion of Effort B.

Preliminary efforts to fabricate sub-10 nm nanowires using W(110) single crystal films in collaboration with Alex Belianinov of Oak Ridge National Laboratory have been unsuccessful. This effort was been frustrated by the low sputter yield for W by He ions and by equipment downtime for the NanoFab instrument used for the nanowire fabrication. Current efforts are returning to e-beam lithography of the Ru single crystal films using HSQ resist. The work at MIT by Prof. C. V. Thompson (on a collaborative research project that includes the PIs on this AFOSR project and is funded by NSF and SRC and is complementary to the work under the AFOSR project) has established that crystallographic faceting of the Ru may provide stability for nanowires with $\left(11\bar{2}0\right)$ orientation. This will be explored in post-patterning anneals of the nanowires. Additional thinning of the e-beam fabricated nanowires by focused ion beam milling and by electrolytic techniques will be explored.

Effort B) Defect and Structural Characterization

X-ray diffraction (XRD) has been an important characterization technique for the single crystal Ru films. Figures 3-5 are examples of XRD patterns for films of all three primary single crystal orientations of Ru on sapphire prepared by the Coffey group. The c-axis in-plane orientations (Figs. 4 and 5) are notable as this is the first time these orientations have been achieved.

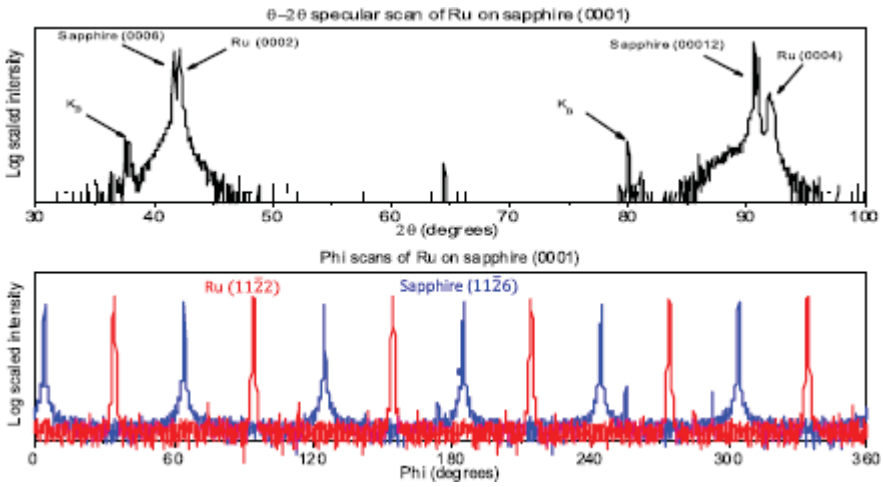

Fig. 3 – (Top) Specular x-ray diffraction scan showing Ru (0002) and sapphire (0006) planes parallel to the substrate surface. (Bottom) Non-specular phi scans showing a 30° difference of the in-plane crystallographic orientation of the Ru and sapphire.

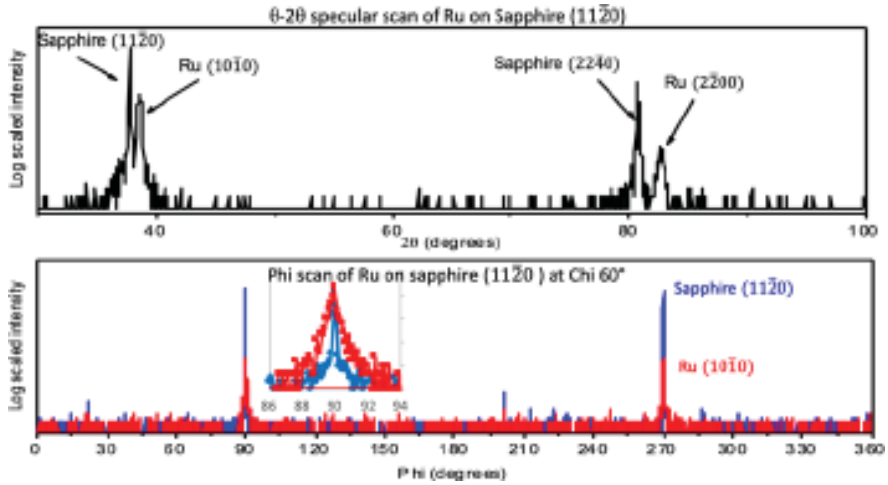

Fig. 4 – (Top) Specular X-ray diffraction scan showing Ru (10$\bar{1}$0) and sapphire (11$\bar{2}$0) planes parallel to the substrate surface. (Bottom) Non-specular phi scans showing a common orientation of the other members of these two families of planes in the sample plane.

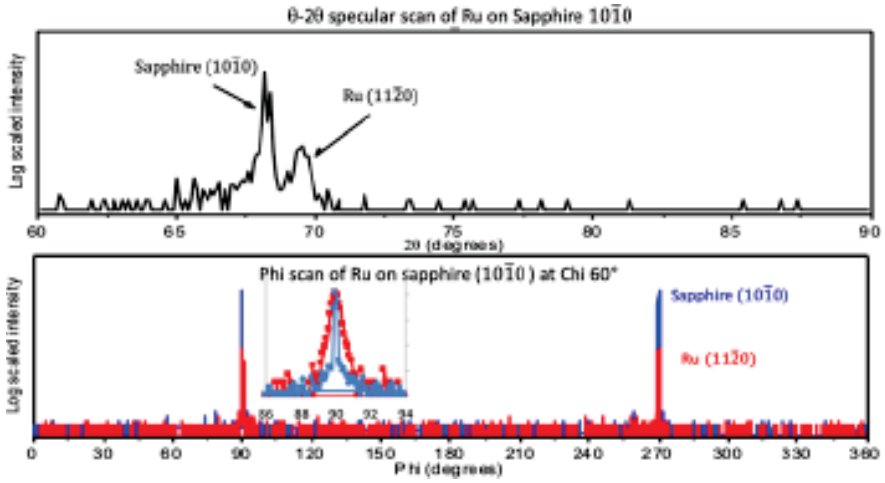

Fig. 5 – (Top) Specular X-ray diffraction scan showing Ru (11$\bar{2}$0) and sapphire (10$\bar{1}$0) planes parallel to the substrate surface. (Bottom) Non-specular phi scans showing a common orientation of other members of these two families of planes in the sample plane.

Low energy electron diffraction (LEED) has also been an important characterization technique for the single crystal character and for the surface quality of the deposited films. This has, surprisingly, been useful for Ru single crystal films that have been air exposed and not cleaned upon introduction to the UHV chamber for LEED characterization. Figure 6 shows a comparison of LEED images obtained from such air-exposed films to an image obtained from a UHV ion beam cleaned and annealed film.

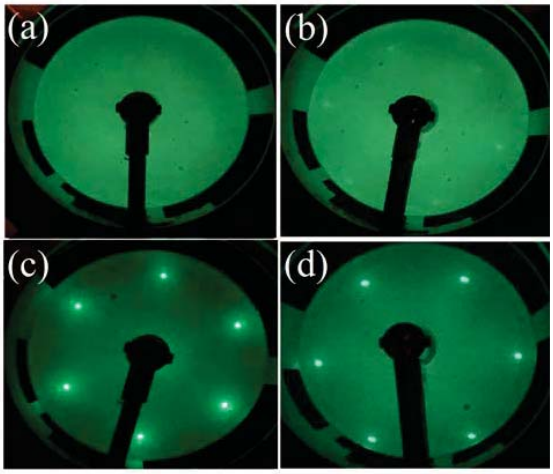

Fig. 6 – LEED images at 68 eV for an air exposed Ru film (a) after deposition at 350 °C, (b) after deposition at 700 °C, (c) after deposition at 700 °C and ex-situ annealing to 950 °C in Ar-3%H_2, and (d) a sample Ar ion beam cleaned and annealed to 1000 °C in UHV conditions with an H_2 background.

Following several sample-holding modifications, the Kaden group has established methods for reliable growth of ordered SiO_2 capping layers on Ru/sapphire(0001) samples provided by the Coffey group. A LEED image taken from a recently produced sample covered by a bilayer sheet of moderately ordered silica is provided in Fig. 7 along with an image of the sample collected during the film crystallization step. X-ray reflectivity (XRR) and X-ray photoelectron spectroscopy (XPS) results obtained from this sample show excellent Ru layer agreement with those noted from hydrogen-annealed

$SiO_x/Ru/Al_2O_3$ samples created with nominally equivalent Ru sheet thicknesses. By contrast, sheet resistance measured from this sample was dramatically higher than that observed from any of the amorphous silica-capped films created by the Coffey group on nominally identical Ru films (resistivity for the Ru layer covered by the ultrathin ordered silica was measured to be 12.6 μΩcm). Based on visual inspection, our working hypothesis is that the mechanical front contacts used to hold the samples in UHV have damaged the Ru thin films, and that this damage is responsible for the bulk of the change in resistivity after growing the SiO_2 thin-films with the Kaden group's UHV system. To circumvent this problem in forthcoming experiments, several masks have been designed so that the Kaden group may make front contacts needed to carry out film growth procedures with their UHV chamber, but without damaging Van der Pauw measured areas of the sheet.

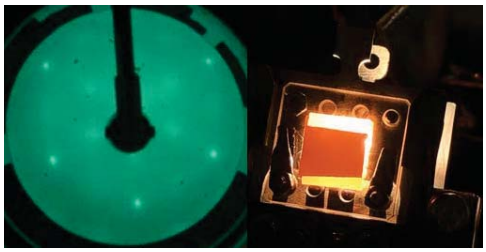

Fig. 7 – (Left) a LEED image exhibiting a weak 2×2 pattern associated with the presence of a bilayer SiO2 honeycomb sheet grown above a 20 nm thick Ru(0001) terminated film. (Right) A picture of the sample taken during film crystallization to highlight the front contacts used as both a mechanical and electronic contact to the Ru samples

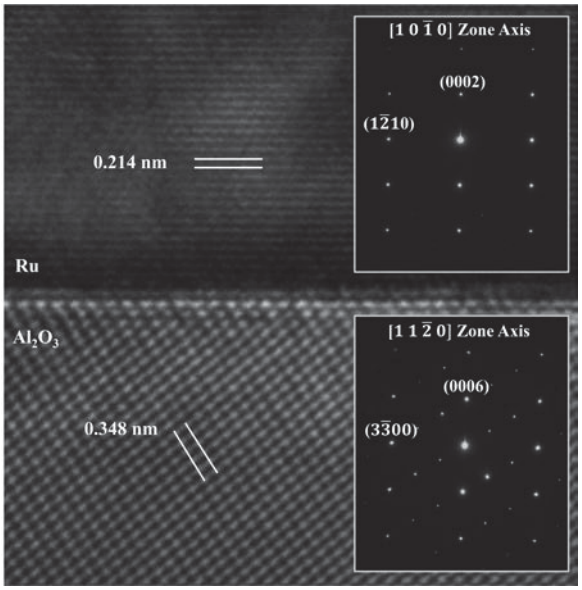

Fig. 8 – High resolution transmission electron micrograph and selected area diffraction patterns of the *in situ* annealed nominally 80 nm-thick Ru film.

Transmission and scanning transmission electron microscopy (S/TEM) characterization of the epitaxial Ru films was carried out by the Barmak group. For most of the cross-sectional samples, the direction normal to the prepared section was parallel to $\left[11\bar{2}0\right]$ in sapphire and thus to $\left[10\bar{1}0\right]$ in Ru. In other words, the sections were prepared parallel to the trace of the $\left(11\bar{2}0\right)$ plane in sapphire and thus the trace of the $\left(10\bar{1}0\right)$ plane in the Ru layers as a result of the 30-degree in plane rotation of the metal layer relative to the sapphire substrate that is adopted in order to minimize the misfit strain.[8]

Epitaxial growth of Ru on c-plane sapphire was shown by XRD, as seen in Fig. 3. This epitaxial growth is further evidenced in Fig. 8, which presents the high-resolution TEM (HRTEM) image of the nominally 80-nm thick (measured thickness of 77.8 nm) Ru film prepared by the Gall group

(on a collaborative research project that includes the PIs on this AFOSR project and is funded by NSF and SRC and is complementary to the work under the AFOSR project) . The (0002) planes of Ru parallel to the Ru/sapphire interface are clearly seen and show the expected interplanar spacing of 0.214 nm. The interplanar spacing in the sapphire substrate of 0.348 nm represents the spacing for the $(1\,\bar{1}02)$ planes at the expected angle of 57.6° to the Ru/sapphire interface for the c-plane sapphire. The insets in Fig. 8 are the selected area electron diffraction patterns for the $[10\,\bar{1}0]$ zone axis in Ru and the $[11\bar{2}0]$ zone axis in sapphire that would have been expected for the choice of sample thinning direction and confirm the orientation relationship determined by XRD, namely $(0001)\,\mathrm{Ru} \parallel (0001)\,\mathrm{sapphire}$ and $[11\bar{2}0]\,\mathrm{Ru} \parallel [1\,\bar{1}00]\,\mathrm{sapphire}$.

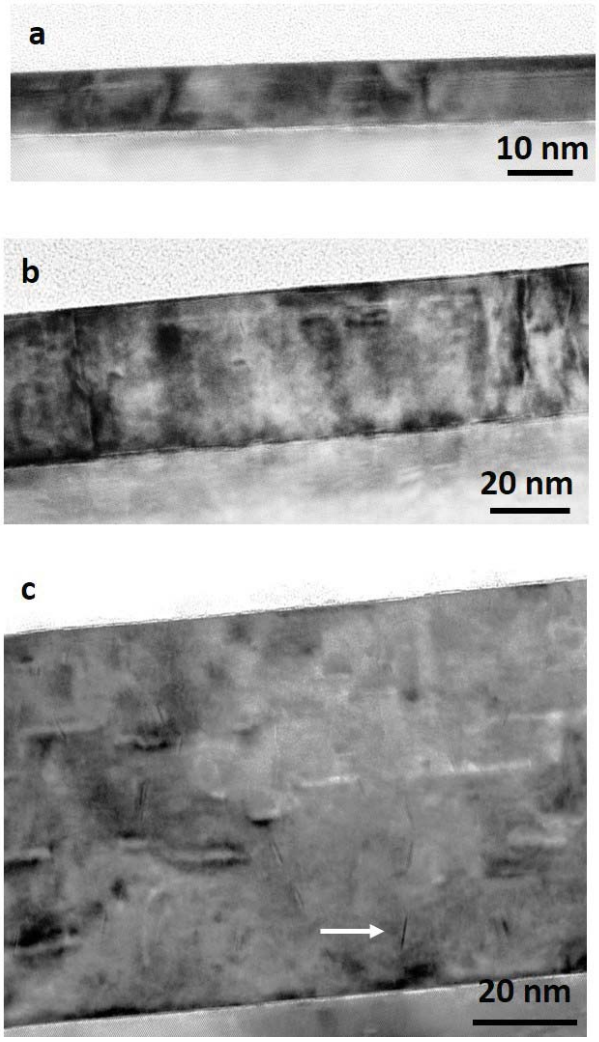

Fig. 9 – High resolution transmission electron micrographs of the cross section of the epitaxial Ru films with nominal thicknesses of (a) 10, (b) 40, (c) 80 nm deposited on c-plane sapphire, prepared parallel to the trace of the Ru $(10\,\bar{1}0)$ and imaged close to the Ru $[10\,\bar{1}0]$ zone axis.

Figures 9a-c show lower magnification high resolution TEM images of the *in situ* annealed 10, 40, and 80 nm thick films, respectively, prepared by the Gall group. Presence of defects at an angle to the basal plane in the 80 nm thick film in Fig. 9c, one of which is marked with an arrow, is clearly seen. The basal plane is parallel to the Ru/sapphire interface in the image. In addition to these defects seen at an angle to the basal plane there are a number of defects seen parallel to the basal plane. These defects are more clearly visualized in the weak beam dark field image presented in Fig. 11. The 40 nm-thick Ru film in Fig. 9b shows similar types of defects to the 80 nm thick film, but the density of defects appears lower. The 10 nm-thick film shown in Fig. 9a appears to have no defects.

The Ru films annealed at 700 °C prepared by the Coffey group showed similar types of defects to the ones seen in the films prepared by the Gall group. However, their density appeared to be higher

at a given thickness and the films contained another type of defect with a hexagonal outline that were not seen in the films from the Gall group, when viewed along the $\left[10\bar{1}0\right]$ zone axis in Ru.

Bright field, dark field, weak-beam dark field (WBDF) and high-resolution transmission electron microscopy (TEM) were used to further characterize the defect structure of the 80-nm thick Ru(0001) film. The selected area diffraction patterns for Ru$\left[10\bar{1}0\right]$ and Ru$\left[11\bar{2}0\right]$ viewing directions are shown in Figs. 10 a and b, respectively. The different diffraction spots (diffraction vectors, **g**) are identified. Based on the combination of imaging methods and simulations, the defects in the Ru layer can be divided into four distinct types: (i) misfit dislocations, (ii) threading dislocations, (iii) deformation twins, and (iv) basal plane defects, as detailed below. [11-16]

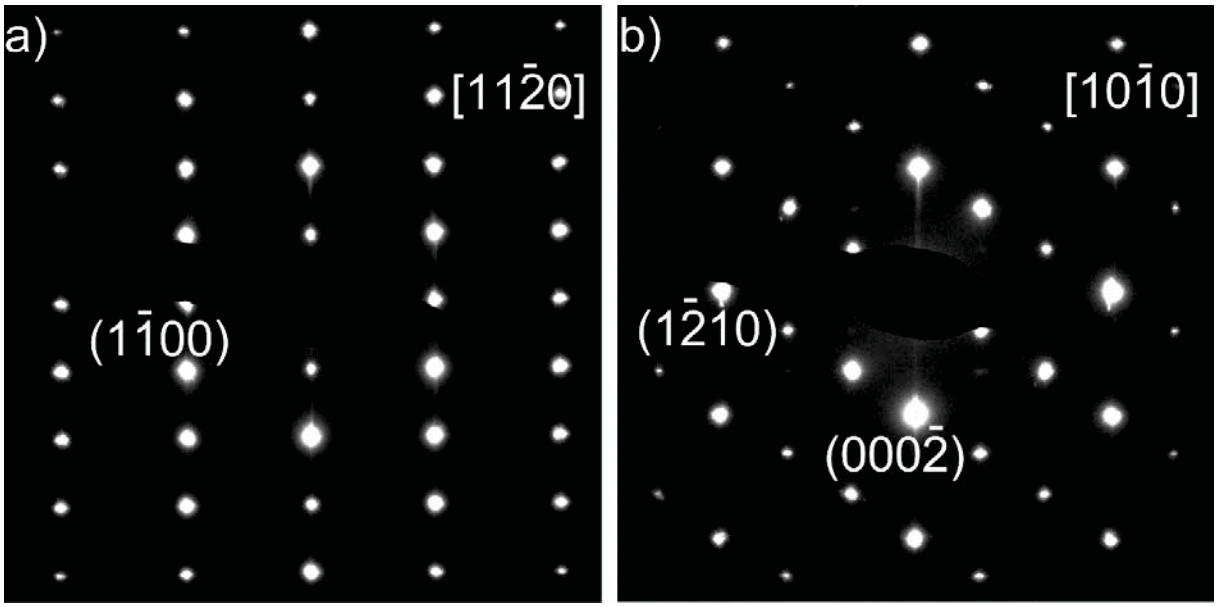

Fig. 10 - Electron diffraction patterns from two different zone axis of Ru and Sapphire substrate, a) $\left[11\bar{2}0\right]$ and b) $\left[10\bar{1}0\right]$.

The first type of defects, the misfit dislocations, form as a result of the 1.6% lattice mismatch between Ru and Al_2O_3 for the 30-degree rotated epitaxial relationship once the film is thick enough to relax by formation of these dislocation. A high density of these dislocations, located at the interface between Ru and Al_2O_3, was observed. These defects can be seen with bright contrast at the interface region in Fig. 11a. A high-resolution transmission electron micrograph (HRTEM) image from Ru/Sapphire interface is shown in Fig. 12a. The Fourier filtered image of this figure in given in Fig. 12b for a given spatial frequency and clearly reveals the extra half plane in the interface for an edge misfit dislocation inside the grey box.

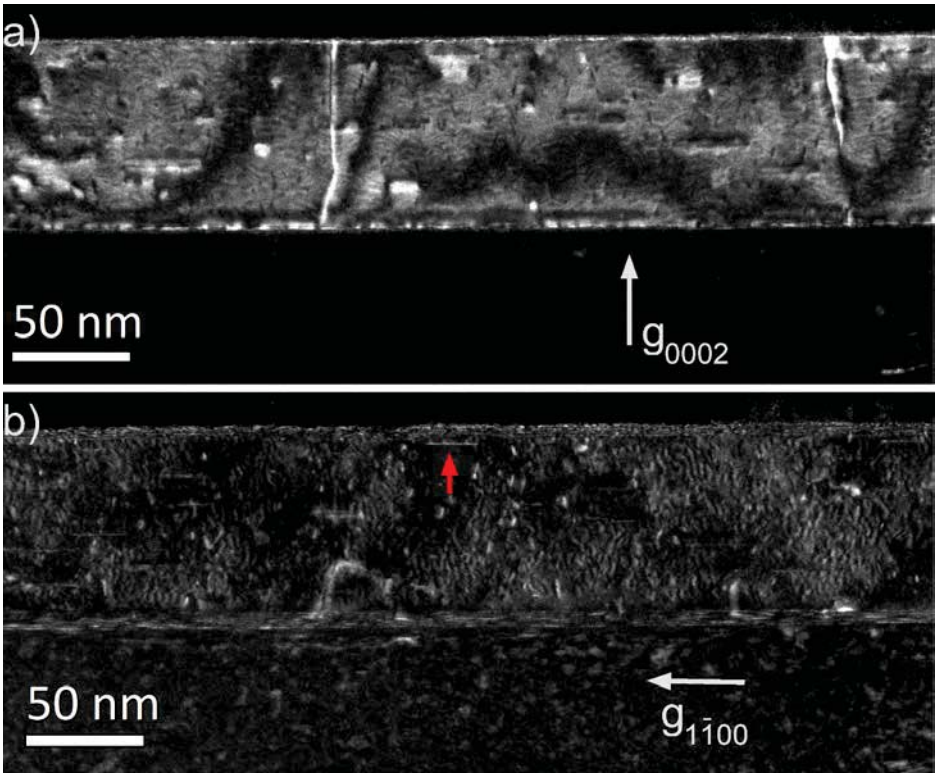

Fig. 11 - WBDF (**g/3g**) image acquired close to $\left[1\bar{1}\bar{2}0\right]$ zone axis. Two different reciprocal lattice vectors perpendicular to each other are selected for imaging (a) $\mathbf{g}_{0002}$ and (b) $\mathbf{g}_{10\bar{1}0}$.

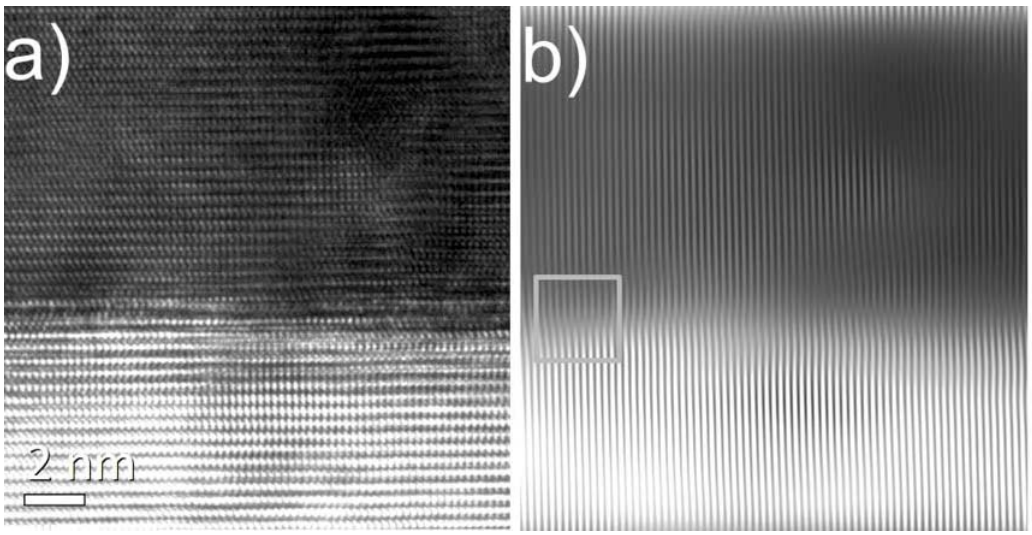

Fig. 12 - (a) HRTEM image acquired along Ru/Sapphire interface. (b) Fourier filtered image of (a) showing a misfit dislocation at the interface inside the grey box.

The second type of dislocations, the threading dislocations, were characterized based on '**g**.**b**' visibility criteria, by taking into account the WBDF images from both orientations of cross-section samples. Here, **g** again refers to the diffraction vector or the diffracted beam selected for imaging and **b** is the Burgers vector of the dislocation that defines the magnitude and direction of slip. Table 3 gives a summary of the visibility criteria (i.e., whether the dislocation of with a given type of Burgers vector is expected to be visible) for the given **g** vector. Based on these criteria, the threading dislocations are identified as having a Burgers vector of <0001> type or <**c**> type. These dislocations seen as white lines traversing the film thickness in Fig. 11a. They are invisible in Fig. 11b. Some segments of the threading dislocations are also clearly along the **c**-axis, i.e., normal to the substrate, and are pure screw type dislocations. The line segments that are at a significant angle to the Ru **c**-axis should then be of the mixed type (i.e., with both screw and edge components). However, these dislocations did not fully satisfy the expected visibility criteria, so our identification of their type as mixed type is based on their angle with the **c**-axis of the film.

Table 3. Diffraction and visibility conditions in this study.

	<**a**> dislocations		<**c**> dislocations	<**c+a**> dislocations	
	b = 1/3 <11-20>	Shockley partials **b** = 1/3 <10-10>	**b** = <0001>	**b** = 1/3 <11-23>	Frank partials, **b** = 1/6 <20-23>
g = [0001]	Invisible	Invisible	Visible	Visible	Visible
g = [1-210]	Visible	Visible except **b** = 1/3 [10-10]	Invisible	Visible	Visible except **b** = 1/6 [20-23]
g = [1-100]	Visible except **b** = 1/3 [11-20]	Visible	Invisible	Visible except **b** = 1/3 [11-23]	Visible

For the third type of defects, the deformation twins, high resolution imaging, trace analysis and image simulation were used to identify the twin system, i.e. the twinning plane and the twinning direction. Epitaxial films commonly relax the misfit strain via the formation of misfit and threading screw dislocations. Deformation twinning is an alternative plastic deformation mode to slip, i.e., deformation by creation and motion of dislocations. In the classical theory of deformation twinning [16], the original (parent) lattice is re-oriented by atom displacements which are equivalent to a simple shear of the lattice points, or some integral fraction of these points. The invariant plane of shear is called $\mathbf{K}_1$ and the shear direction $\boldsymbol{\eta}_1$. The second undistorted (or conjugate) plane is $\mathbf{K}_2$. The plane containing $\boldsymbol{\eta}_1$ and the normals to $\mathbf{K}_1$ and $\mathbf{K}_2$ is the plane of shear **P.** The intersection of $\mathbf{K}_2$ and **P** is the conjugate shear direction $\boldsymbol{\eta}_2$. The four $\mathbf{K}_1$, $\boldsymbol{\eta}_1$ twin and their respective $\mathbf{K}_2$, $\boldsymbol{\eta}_2$ conjugate twin systems listed in Table 4 are the most important ones to consider. For type I twins $\mathbf{K}_1$ and $\boldsymbol{\eta}_1$ ($\mathbf{K}_2$ and $\boldsymbol{\eta}_2$) are rational. For compound twins, $\mathbf{K}_1$,$\boldsymbol{\eta}_1$, $\mathbf{K}_2$ and $\boldsymbol{\eta}_2$ are all rational.

To determine which of the twin or conjugate twin systems is consistent with the observed defects in Fig. 9c, the angle between the trace of the defects in the image and the trace of the basal plane was measured for several tens of defects. Crystallographic computation was then used to calculate angle for the trace of the twin and conjugate twin planes listed in Table 4, for the given image plane Ru $\left(10\bar{1}0\right)$. This involved 148 crystallographic computations.

Table 4 – Crystallographic elements and parameters of the compound twin systems in hexagonal Ru with c/a = 1.582. **s** is the magnitude of the shear. See text for more detail. [16]

$\mathbf{K_1}$	$\mathbf{K_2}$	$\boldsymbol{\eta_1}$	$\boldsymbol{\eta_2}$	**s**
$\{10\bar{1}2\}$	$\{10\bar{1}\bar{2}\}$	$\pm\langle 10\bar{1}1\rangle$	$\pm\frac{1}{3}\langle 1\bar{2}10\rangle$	0.18
$\{10\bar{1}1\}$	$\{10\bar{1}\bar{3}\}$	$\langle 30\bar{3}2\rangle$	$\frac{1}{3}\langle 1\bar{2}10\rangle$	0.09
$\{11\bar{2}2\}$	$\{11\bar{2}4\}$	$\frac{1}{3}\langle 22\bar{4}3\rangle$	$\langle 1\bar{1}00\rangle$	0.21
$\{11\bar{2}1\}$	$\{0002\}$	$\frac{1}{3}\langle\bar{1}\bar{1}26\rangle$	$\frac{1}{3}\langle 11\bar{2}0\rangle$	0.63

The computed values of the angles were compared with experimentally measured values. Experimentally measured values were 14.7° ± 2.1° (34 twins traces measured in three Ru $\left(10\bar{1}0\right)$ image plane). This value is closest to the computed value of 17.5° (next closest was 32.3°). Therefore, we concluded that the defects at an angle to the basal plane are the "compression" twin $\{11\bar{2}1\}\frac{1}{3}\langle\bar{1}\bar{1}26\rangle$. (We note that the computed value of the angle is outside of the standard deviation of the experimental values, but this may well be because the sample is not exactly on zone axis for Ru, though it is exactly on zone axis for sapphire). "Compression" refers to compressive strain along the c-axis. Equivalently, the twin would form by "tension" normal to the c-axis. This tensile strain is consistent with the 1.5% tensile misfit strain for Ru films deposited on c-plane sapphire. XRD measurements of the c-lattice parameter of the nominally 80 nm thick Ru film by the Gall group shows a fully relaxed film. We concluded that this strain relaxation is a result of the formation of the twin defects.

Two interesting features of the $\{11\bar{2}1\}\frac{1}{3}\langle\bar{1}\bar{1}26\rangle$ twin system are that: (i) this twin system requires zero lattice shuffles, though the shear is the highest, (ii) the conjugate twin system, the basal plane twin $\{0002\}\frac{1}{3}\langle 11\bar{2}0\rangle$, is also a known slip system. Basal plane defects in the 80 nm-thick Ru film are clearly seen in Figs. 9 and 11. Since the formation of deformation twins is either preceded by

or accompanied by the formation of dislocations, the threading dislocations may well be associated with twinning in these films.

In addition to the trace analysis to identify the deformation twins, electron diffraction simulation study was performed and the result was compared with Fourier transform of the HRTEM image given in Fig. 13a. For the simulation, first a Ru crystal with a twin described above was generated. The size of Ru crystal is 2.3 nm × 4.1 nm × 6.7 nm. A simulated HRTEM image of such crystal is given in Fig.13b. For both the HRTEM image and electron diffraction pattern simulation MulTem has been used [14]. The simulated diffraction pattern is given as an inset in Fig. 18b. Comparison of the Fourier Transform (inset Fig. 18a) of the HRTEM micrograph and the simulated electron diffraction pattern from the Ru crystal (inset of Fig. 18b) clearly shows the streaks along the same direction on the patterns. Based on this simulation study, we can confirm the twinning elements of the twin observed are as listed above, i.e., $\{11\bar{2}1\}\frac{1}{3}\langle\bar{1}\,\bar{1}26\rangle$. Deformation twinning is an important mechanism for strain relaxation in crystals of lower symmetry.[16]

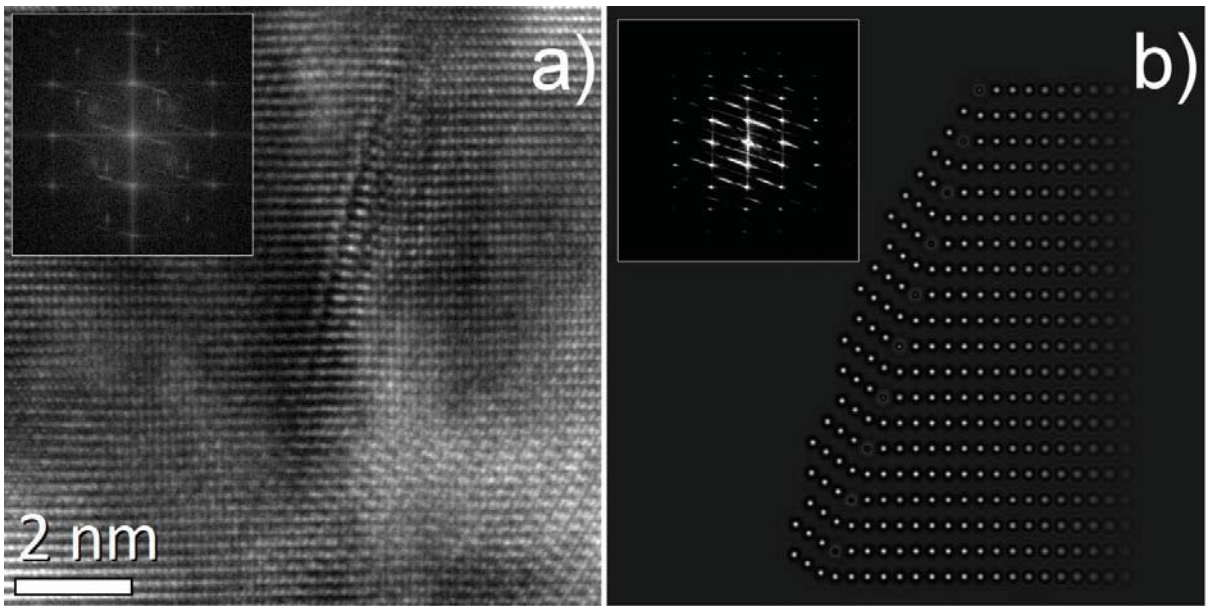

Fig. 13 – (a) High resolution transmission electron micrograph image along $\left[10\bar{1}0\right]$ zone axis of the 80-nm thick Ru film prepared by the Gall group and its Fourier transform (inset). (b) Simulated $\{11\bar{2}1\}\frac{1}{3}\langle\bar{1}\,\bar{1}26\rangle$ deformation twin structure and diffraction pattern (inset).

The fourth type of defects, the basal plane defects are yet to be fully identified. The difficulty with the identification of defects is that they are extremely thin and so cannot be identified using usual dark-field imaging techniques, and image simulations as was done for the deformation twins have not been conclusive in unambiguously evidencing the atom displacements. However, our

hypothesis is that these basal plane defects are the conjugate twins to the deformation twins, and thus of the $\{0002\}\frac{1}{3}\langle 11\bar{2}0\rangle$ type. Many of these defects are seen with bright contrast in Fig. 11 a. One such defect is marked with the red arrow in Fig. 11b.

Effort C) Computational Modeling of Nanowire Physics

In the early part of the computational effort, we used the NRL transport models with the pybinding code [17] and the KWANT code [18]. More recently, we began exploration of the KITE quantum transport software [19], which we were able to interface with models built using pybinding. However, we discovered that these codes were not flexible enough to allow for some of the desired modeling tasks, including especially adding thermal disorder (i.e. phonon vibrations). Inclusion of phonon vibrations is important for describing thermoelectric performance.

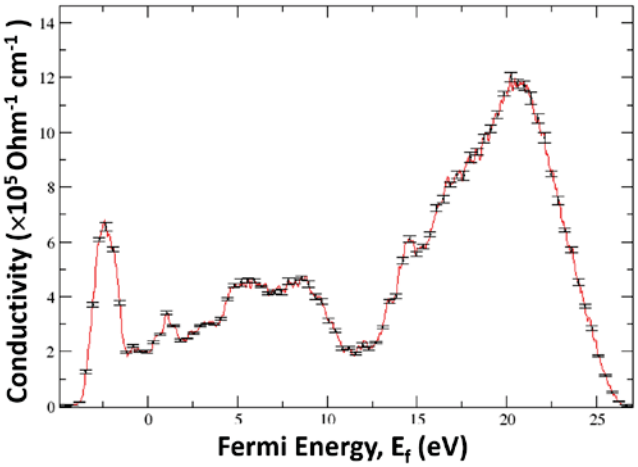

Fig. 14 – Computed conductivity of a 70 nm long wire, with approximate transverse dimensions 4 nm × 4 nm. The results are obtained for different selections of the Fermi energy. The actual Fermi energy was determined to be about 2.8 eV. Error bars represent statistical averaging over a large number of initial random vectors.

During the course of the grant period, we developed and optimized our own "in-house" code for the transport calculations. The code implements the Kernel-Polynomial method [20] very efficiently, using an approach which scales linearly with the number of atomic sites. The code has been parallelized to run on very large systems. Several preliminary calculations have been performed using the code, and currently we are working to provide more model validation before publishing. These details are described below.

We first tested the model for a ~70nm long nanowire with approximately 4nm × 4 nm cross section. Transport is along a $[11\bar{2}0]$ direction and no disorder is introduced. The main task was to determine whether for a given number of moments of the KPM expansion, the computed conductivity was comparable to experimental values, and also to establish good convergence of the results with the number of random vectors used for trace computations. We obtained the results shown in Fig. 14 which shows good-order-of-magnitude agreement with experiment, and also excellent convergence for ~12 random vectors. We have computed conductivities for wires with

up to 10^6 sites, with calculations taking just a few hours to run when the number of processors was chosen equal to the number of random initial vectors for parallelization.

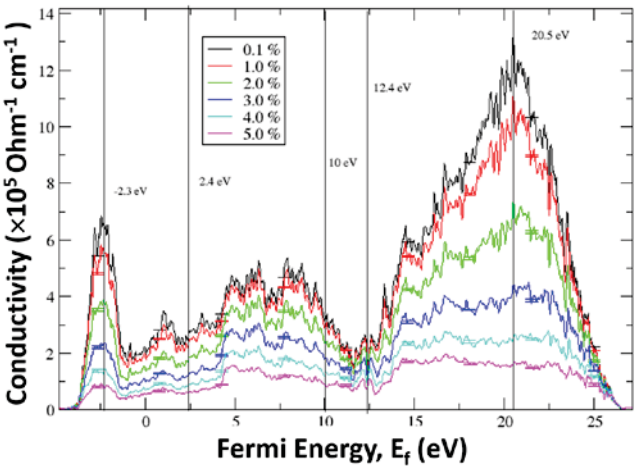

Fig. 15 – Computed conductivity for different amounts of random atomic displacement.

We have significant preliminary results to understand how conductivity scale with thermal noise and surface roughness, although we are yet to determine how the conductivity scales with wire diameter, which is one of the main objectives of the project. In Fig. 15, we show preliminary results for the dependence on thermal noise, represented here with atomic displacements characterized as a fraction of lattice parameter. Strong decreases in conductivity are evident with increasing thermal noise for the same nanowire explored in Fig. 14. However, there is no evidence for Anderson localization in the preliminary calculations.

In addition, we have developed an algorithm to introduce random surface roughness into the wires, and this has been included in a preliminary study. The algorithm introduces random roughness, with variable wavelengths and amplitudes. In Fig. 16, we show a typical rough nanowire structure, and in Fig. 17 we show the computed conductivity. As expected, the rough wire, even without any added thermal noise, exhibits significantly decreased conductivity.

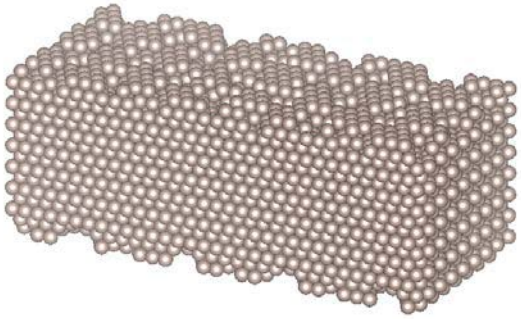

Fig. 16 – Initial structure for studies of the effect of surface roughness on electronic conductivity.

We are now in a position where we can generate large amounts of data to obtain information on the conductivity for different roughness, diameter, orientation, and thermal noise. We have partially validated the tight-binding model. With support from other grants, we intend to refit the model. Finally, we expect that only minor additions to the existing computer code will enable calculation of the Seebeck coefficients and consequently thermoelectric properties.

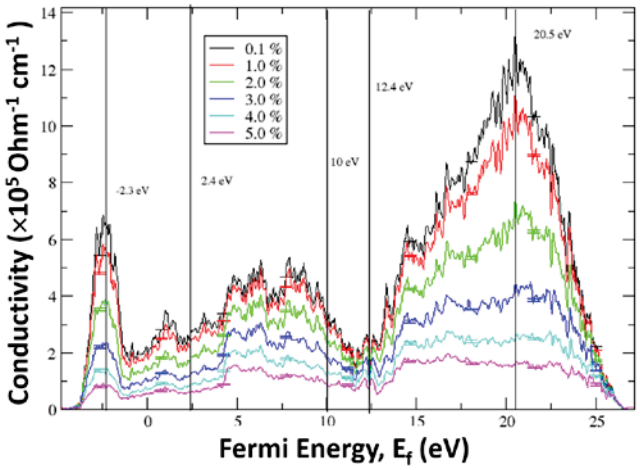

Fig. 17 – Computed conductivity for the rough wires shown in Fig. 3 in comparison to the conductivity.

References

1. K. M. Schep, P. J. Kelly, and G. E. W. Bauer, *Ballistic transport and electronic structure*, Phys. Rev. B 57, 8907 – 8926 (1998).
2. P. Poncharal, C. Berger , Y. Yi , Z. L. Wang , and W. A. de Heer, *Room Temperature Ballistic Conduction in Carbon Nanotubes*, J. Phys. Chem. B, 106, 12104–12118 (2002)
3. K. Fuchs, *The conductivity of thin metallic films according to the electron theory of metals,* Mat. Proceedings of the Cambridge Philosophic Society 34, 100-108 (1938).
4. E. H. Sondheimer, *The mean free path of electrons in metals.* Advances in Physics 50, 499-537 (2001).
5. A. F. Mayadas, and M. Shatzkes, *Electrical-Resistivity Model for Polycrystalline Films - Case of Arbitrary Reflection at External Surfaces.* Physical Review B 1, 1382-1389 (1970).
6. A. F. Mayadas, M. Shatzkes, and Chaudhary. P, *Electron Scattering at Grain-Boundaries in Thin Metal Films.* Bulletin of the American Physical Society, 15, 252 (1970).
7. A. F. Mayadas, M. Shatzkes, and J.F. Janak, *Electrical Resistivity Model for Polycrystalline Films - Case of Specular Reflection at External Surfaces.* Applied Physics Letters, 14, 345-347 (1969).
8. A Satoru Yamada, Yuki Nishibe, Masato Saizaki, Hiromichi Kitajima, Shigeru Ohtsubo, Akiharu Morimoto, Tatsuo Shimizu, Katsuei Ishida and Yuichi MASAKI, *Rotational Honeycomb Epitaxy of Ru Thin Films on Sapphire (0001) Substrate*, Japanese Journal of Applied Physics **41**, 206 (2002).
9. S. S. Ezzat, P. D. Mani, A. Khaniya, W. Kaden, D. Gall, K. Barmak, K. R. Coffey, "Resistivity and surface scattering of (0001) single crystal ruthenium thin films," Journal of Vacuum Science & Technology A 37, 031516 (2019).
10. B. Yang, W. E. Kaden, X. Yu, J. A. Boscoboinik, Y. Martynova, L. Lichtenstein, M. Heyde, M. Sterrer, R. Włodarczyk, M. Sierka, J. Sauer, S. Shaikhutdinov, H.-J. Freund, *Thin silica films on Ru (0001): monolayer, bilayer and three-dimensional networks of [SiO_4] tetrahedra*, Physical Chemistrty Chemical Physics **14,** 11344-11351 (2012).

11. Manasreh, Mahmoud Omar, ed. III-nitride semiconductors: electrical, structural and defects properties. Elsevier, 2000.
12. Zhang, Dalong, et al. "TEM study on relationship between stacking faults and non-basal dislocations in Mg." Philosophical Magazine 95.34 (2015): 3823-3844.
13. Kohn, Simon C. "CrystalMaker: Interactive Crystallography." *Terra Nova* 7.5 (1995): 554-556.
14. Lobato, I., and D. Van Dyck. "MULTEM: A new multislice program to perform accurate and fast electron diffraction and imaging simulations using Graphics Processing Units with CUDA." *Ultramicroscopy* 156 (2015): 9-17.
15. Sears, V. F., and S. A. Shelley. "Debye–Waller factor for elemental crystals." *Acta Crystallographica Section A* 47.4 (1991): 441-446.
16. Christian, John Wyrill, and Subhash Mahajan. "Deformation twinning." *Progress in materials science* 39.1-2 (1995): 1-157.
17. http://docs.pybinding.site/en/stable/
18. https://kwant-project.org/
19. https://quantum-kite.com
20. [11] D. Mayou, and S.N. Khanna, *A Real-Space Approach to Electronic Transport,* Journal De Physique I 5, 1199-1211 (1995).